Electronic spin polarization with an optical centrifuge

Johannes Floß
Chemical Physics Theory Group, Department of Chemistry, and Center for Quantum Information and Quantum Control, University of Toronto, Toronto, Ontario, Canada M5S 3H6

Christian Boulet
Institut des Sciences Moléculaires d'Orsay (ISMO), CNRS, Université Paris-Sud, Université Paris-Saclay, F-91405 Orsay, France

Jean-Michel Hartmann
Laboratoire de Météorologie Dynamique/IPSL, CNRS, Ecole polytechnique, Université Paris-Saclay, 91128 Palaiseau, France

Alexander A. Milner and Valery Milner
Department of Physics and Astronomy, University of British Columbia, Vancouver, Canada V6T 1Z1

(Received 27 June 2018; published 1 October 2018)

We investigate, both theoretically and experimentally, the mechanism behind the creation of a macroscopic magnetization in a gas of paramagnetic molecules with an optical centrifuge, reported in [Phys. Rev. Lett. **118**, 243201 (2017)]. Our analysis shows that the centrifuged super-rotors and noncentrifuged molecules are polarized in opposite directions, while the net magnetic moment of the whole ensemble at the end of the interaction with the laser pulse remains close to zero. As the super-rotors are more stable against reorienting collisions, their spin polarization, which points along the centrifuge axis, decays more slowly than the oppositely oriented polarization of the noncentrifuged molecules. The latter lose their directional rotation much more quickly and with it the polarization of their electronic spin. We show numerically that owing to this difference in decay rates, a net magnetization in the direction of the centrifuge is generated. The proposed model is supported by experimental data.

DOI: 10.1103/PhysRevA.98.043401

I. INTRODUCTION

Molecular super-rotors are molecules in extremely high rotational states. They can be created by means of an optical centrifuge, which uses a superposition of two oppositely chirped circularly polarized laser pulses to create an optical field with rotating linear polarization [1,2]. The rotational energy of super-rotors is much greater than their vibrational energy and can even become comparable to the energy of electronic excitations. This inversion of the energy scales can lead to many interesting effects. Most relevant to this work, super-rotor states are more stable against collisions than their slow counterparts, which leads to the formation of long-lived molecular gyroscopes [3–6].

Coupling between the nonzero electronic spin and the molecular rotation in paramagnetic super-rotors, like O_2, provides a powerful tool for controlling both the molecular rotation and the molecular magnetism. Recent studies showed that this coupling is sufficiently strong for an external magnetic field to flip the axis of molecular rotation or align the molecules along the laboratory axis at ambient conditions [7–9]. In contrast, conventional paramagnetic rotors can be aligned by a laboratory-scale external magnetic field only at temperatures of a few Kelvin [10,11].

It was also recently demonstrated that a magnetic field of the order of tens of milligauss can be induced in a gas of optically centrifuged paramagnetic super-rotors [12]. In that study, a centrifuge laser pulse interacted with O_2 molecules at ambient conditions and an induced gas magnetization was observed along the centrifuge axis. The dynamics of the induced magnetic moment depended on the gas pressure, indicating that collisions may be responsible for the observed effect, yet no clear mechanism was provided. This warranted a more detailed study of the centrifuge-induced magnetization of paramagnetic super-rotors. The results of this study are presented here.

The paper is split into three main parts. In the first one, presented in Sec. II, we investigate numerically the ability of an optical centrifuge to polarize the electronic spin of a paramagnetic molecule in the absence of collisional relaxation. In Sec. III, we use the result of the above analysis and evaluate the role of collisions in creating macroscopic spin polarization. Finally, the results of numerical calculations are compared with our experimental findings in Sec. IV.

II. SPIN POLARIZATION IN THE ABSENCE OF COLLISIONS

A. Theoretical model and numerical methods

We start by investigating the polarization of the electronic spin induced during the interaction of a molecule with the centrifuge pulse. Since in our experiments the latter is shorter than the average time between collisions (>100 ps for oxygen under ambient conditions), collisional relaxation is ignored. We consider the following scenario: An optical centrifuge

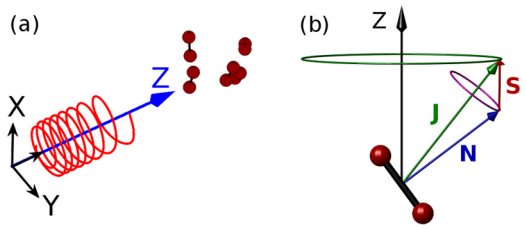

FIG. 1. (a) Considered interaction geometry. A centrifuge laser pulse with rotating linear polarization (red spiraling line) interacts with oxygen molecules. The propagation axis of the laser defines the laboratory Z axis. The angular momentum of the excited molecules is oriented along this axis. (b) Angular momentum coupling in an arbitrarily rotating (noncentrifuged) O_2 molecule. The orbital angular momentum $\mathbf{N}$ couples with the electronic spin $\mathbf{S}$ to form the total angular momentum $\mathbf{J}$. This coupling leads to three nondegenerate states with $J = N - 1$, $J = N$, and $J = N + 1$ (only the latter is pictured for clarity).

pulse interacts with an ensemble of $^{16}O_2$ molecules and excites them to very fast rotation in the direction of the centrifuge. The geometry of the interaction is depicted in Fig. 1(a). Note that the laser propagation axis defines the laboratory Z axis and thus the centrifuged molecules acquire a rotational angular momentum pointing along Z. In this section, we investigate whether and how this rotational excitation induces a polarization of the electronic spin $\mathbf{S}$, measured as the projection $\langle M_S \rangle$ of $\mathbf{S}$ onto the Z axis.

The $^3\Sigma_g^-$ electronic ground state of molecular oxygen has an electronic spin of $S = 1$, which leads to spin-rotation coupling between $\mathbf{S}$ and the rotational angular momentum $\mathbf{N}$ [13,14], as shown in Fig. 1(b). As a result of this coupling, $\mathbf{S}$ and $\mathbf{N}$ form the total angular momentum $\mathbf{J} = \mathbf{N} + \mathbf{S}$. Because of the spin multiplicity, every rotational level is split into three nondegenerate spin-rotational states: $J = N + 1$, $J = N$, and $J = N - 1$. Below, we refer to these states as K_+, K_0, and K_-, respectively.

The effective spin-rotational Hamiltonian of oxygen molecules consists of three terms [14–16]:

$$\mathcal{H}_{\text{eff}} = \mathcal{H}_{\text{rot}} + \mathcal{H}_{\text{ss}} + \mathcal{H}_{\text{so}} . \tag{1}$$

Here, $\mathcal{H}_{\text{rot}}$ describes the rotation of the molecule and is given as

$$\mathcal{H}_{\text{rot}} = B_0 \mathbf{N}^2 - D\mathbf{N}^4 , \tag{2}$$

with the rotational and centrifugal distortion constants $B_0 = 1.43\,\text{cm}^{-1}$ and $D = 4.8 \times 10^{-6}\,\text{cm}^{-1}$ [17]. The spin-spin interaction energy,

$$\mathcal{H}_{\text{ss}} = \tfrac{2}{3}\lambda[3S_\zeta^2 - \mathbf{S}^2], \tag{3}$$

depends on the projection of the total electronic spin on the internuclear axis, S_ζ. Here, $\lambda = 1.98\,\text{cm}^{-1}$ [14] is the spin-spin coupling constant. The spin-rotation coupling between the electronic spin and the rotational angular momentum $\mathbf{N}$ is mainly caused by the interaction of $\mathbf{S}$ with the magnetic field of the electrons that follow the rotating nuclei [15]. It can be written as

$$\mathcal{H}_{\text{so}} = \gamma \mathbf{N} \cdot \mathbf{S} , \tag{4}$$

where $\gamma = -0.0083\,\text{cm}^{-1}$ [14]. Note that because of the spin-rotation coupling, N is not a good quantum number. However, the mixing of different N is sufficiently weak, allowing us to use N as a label for different rotational states. Because of the exchange symmetry of the identical nuclei, only odd values of N are allowed.

An optical centrifuge is created by two circularly polarized laser fields of opposite handedness, which are frequency chirped opposite to one another [1,2]. Their interference results in a linearly polarized field,

$$\mathbf{E}(t) = E_0 \mathcal{E}(t) \cos \omega t [\hat{\mathbf{x}} \cos \phi_{\text{L}}(t) + \hat{\mathbf{y}} \sin \phi_{\text{L}}(t)], \tag{5}$$

where E_0 is the peak amplitude, $\mathcal{E}(t)$ is the dimensionless envelope of the laser electric fields, $\hat{\mathbf{y}}$ and $\hat{\mathbf{x}}$ are unit vectors along the laboratory X and Y axes, ω is the central frequency of the laser, and the phase $\phi_{\text{L}}(t)$ is quadratically dependent on time:

$$\phi_{\text{L}}(t) = \frac{\beta}{2} t^2 . \tag{6}$$

The instantaneous polarization axis $\mathbf{p}(t)$ rotates with a constant acceleration $\dot{\phi}_{\text{L}}(t) = \beta$ in the XY plane. The nonresonant (with respect to electronic transitions) laser pulse induces a dipole moment in the molecule via its electric polarizability and then interacts with that induced dipole. Averaging over the fast oscillations of the laser field leads to the following effective interaction potential [18–21]:

$$V(t) = -\frac{\Delta\alpha}{4} E_0^2 \mathcal{E}^2(t) [\mathbf{r} \cdot \mathbf{p}(t)]^2 , \tag{7}$$

where $\Delta\alpha$ is the polarizability anisotropy and $\mathbf{r} = (r_X, r_Y, r_Z)$ is the orientation of the molecular axis. Hereafter, the parameters of the centrifuge pulse were chosen to match the experimental conditions in Ref. [12]: peak intensity of $I_0 = 2\,\text{TW/cm}^2$, frequency chirp of $\beta = 0.52 \times 10^{24}\,\text{s}^{-2}$, turn-on and turn-off times of 2 ps, and duration between 30 and 80 ps. Depending on the latter parameter, this centrifuge field excites angular momenta of O_2 between $33\,\hbar$ and $83\,\hbar$. For clarity, a righthanded centrifuge pulse is considered, resulting in a positive projection of $\mathbf{N}$ onto the laboratory Z axis.

To calculate the molecular spin polarization, the evolution of the wave function expressed in Hund's case (b) basis, $|\Psi\rangle \equiv |J, N, M\rangle$, is calculated by solving the time-dependent Schrödinger equation (see Appendix A for details),

$$i\hbar \frac{\partial |\Psi\rangle}{\partial t} = [\mathcal{H}_{\text{eff}} + V(t)]|\Psi\rangle . \tag{8}$$

The spin polarization is defined as the expectation value $\langle M_S \rangle$ of the projection of the electronic spin onto the laboratory Z axis. It is readily obtained from the uncoupled basis $|N, M_N\rangle|S, M_S\rangle$, which is related to the Hund's case (b) basis via [14]

$$|J, N, M\rangle = (-1)^{S-N+M} \sqrt{2J+1} \times \sum_{M_N, M_S} \begin{pmatrix} N & S & J \\ M_N & M_S & -M \end{pmatrix} |N, M_N\rangle|S, M_S\rangle . \tag{9}$$

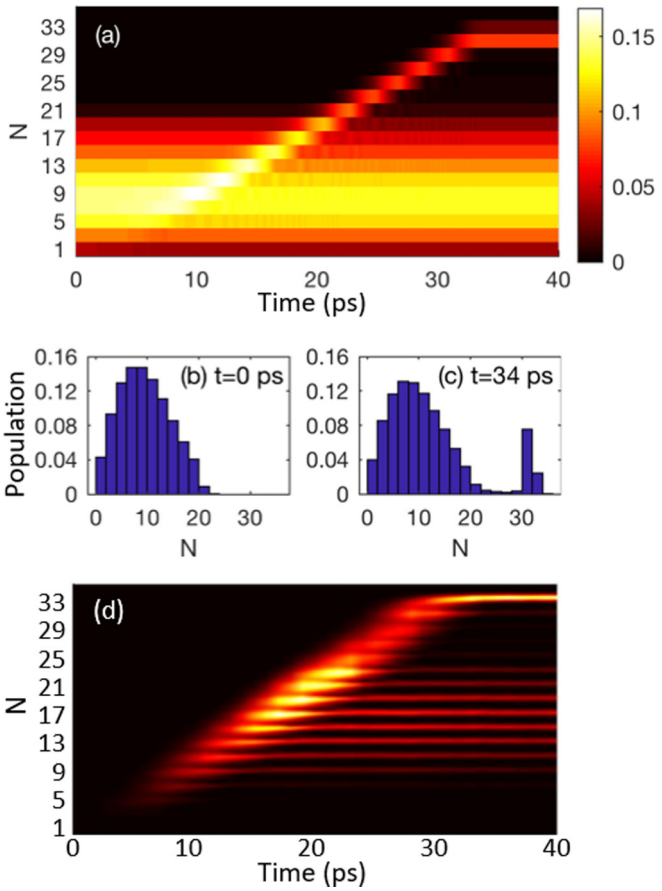

FIG. 2. [(a)–(c)] Calculated populations of the rotational levels N for a thermal ensemble of O_2 molecules interacting with a centrifuge laser pulse of 34-ps duration. Panel (a) shows the full time evolution, whereas panels (b) and (c) are snapshots at the beginning and the end of the laser pulse, respectively. (d) Experimental Raman spectrogram for a 34 ps centrifuge, showing strong excitation of $N = 33$ (details in Sec. IV A).

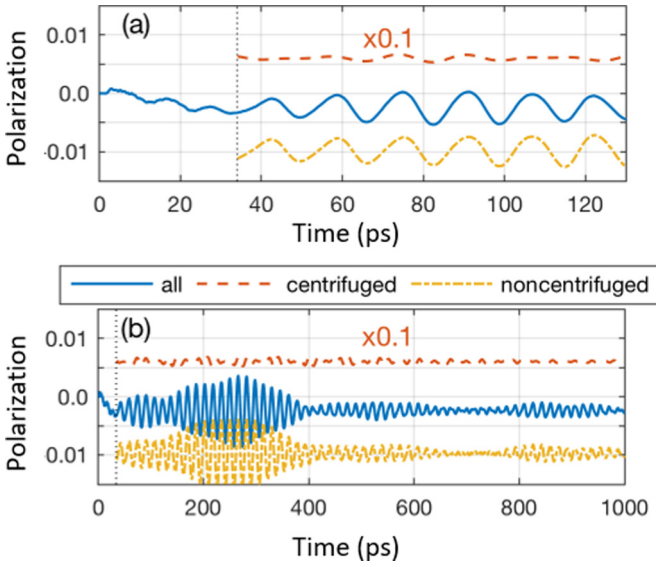

FIG. 3. (a) Polarization of the electronic spin (i.e., expectation value $\langle M_S \rangle$) for a thermal ensemble ($T = 298$ K) of O_2 interacting with a 34-ps-long centrifuge pulse. The end of the pulse is indicated by the dotted vertical line. Shown is the polarization for the whole ensemble (solid blue), as well as its breakdown between centrifuged (red dashed) and noncentrifuged (yellow dot-dashed) molecules, defined as $N > 26$ and $N < 26$, respectively. Note that the polarization of the centrifuged molecules is scaled by a factor of 1/10. (b) Same, but on a longer timescale.

B. Theoretical results: *Centrifuge-induced* spin polarization

Applied to a gas at room temperature, an optical centrifuge captures and spins a fraction of the molecular ensemble. This process is illustrated for O_2 in Fig. 2, where the population of the rotational levels N is shown as a function of time. Figure 2(a) depicts the full time span, whereas Figs. 2(b) and 2(c) show snapshots at the beginning ($t = 0$ ps) and the end ($t = 34$ ps) of the laser pulse. At the beginning, the most thermally populated state is $N = 9$, whereas the total population of rotational levels above $N = 21$ is below 5% and is not included in the analysis to keep the calculation time within reasonable limits. As the polarization vector of the centrifuge rotates more quickly, the rotational frequency of captured molecules is increasing with it, resulting in the diagonal trace in Fig. 2(a). At the end of the laser pulse, the centrifuged molecules are clearly separated in angular momentum from the noncaptured molecules, as reflected by an isolated narrow peak in Fig. 2(c). The centrifuged molecules make up around 10% of the total population and carry rotational angular momenta of $N = 31$. An experimentally recorded Raman spectrogram (see details in Sec. IV A) in Fig. 2(d) demonstrates similar excitation pattern in the measured rotational distribution. Note that the Raman signal is proportional to the modulus squared of the centrifuge-induced rotational coherences, rather than rotational populations calculated and plotted in Fig. 2(a). This explains the difference between the two pictures.

The effect of the centrifuge pulse on the polarization of the electronic spin **S** can be seen in Fig. 3, where the expectation value $\langle M_S \rangle$ is shown on short and long timescales in Figs. 3(a) and 3(b), respectively. For the whole thermal ensemble (solid blue line), one can see that during the laser pulse the molecules become weakly polarized in the negative direction. After the end of the pulse, $\langle M_S \rangle$ oscillates around its average value of -0.0025 with two characteristic periods: a short period of ~17 ps, which corresponds to the splitting of rotational states by the spin-spin interaction, and a long period of ~400 ps, corresponding to the spin-orbit splitting between K_+ and K_- spin states. The split of the total polarization between the centrifuged and noncentrifuged molecules is depicted by red dashed and yellow dash-dotted lines, respectively. The former show positive polarization of 0.06, while the latter are negatively polarized with $\langle M_S \rangle \approx -0.01$. Given that only about 10% of the molecules are centrifuged, the two contributions compensate one another, resulting in a very small net polarization with an absolute magnitude on the order of 10^{-3}.

To understand the mechanism behind the induced separation of spin polarization between centrifuged and noncentrifuged molecules, it is instructive to look separately at the effect of the centrifuge on fast and slow rotors in the initial ensemble. First, consider an oxygen molecule in a high thermally populated initial rotational state, e.g., $N = 11$. Figure 4 illustrates classically the rotational acceleration of

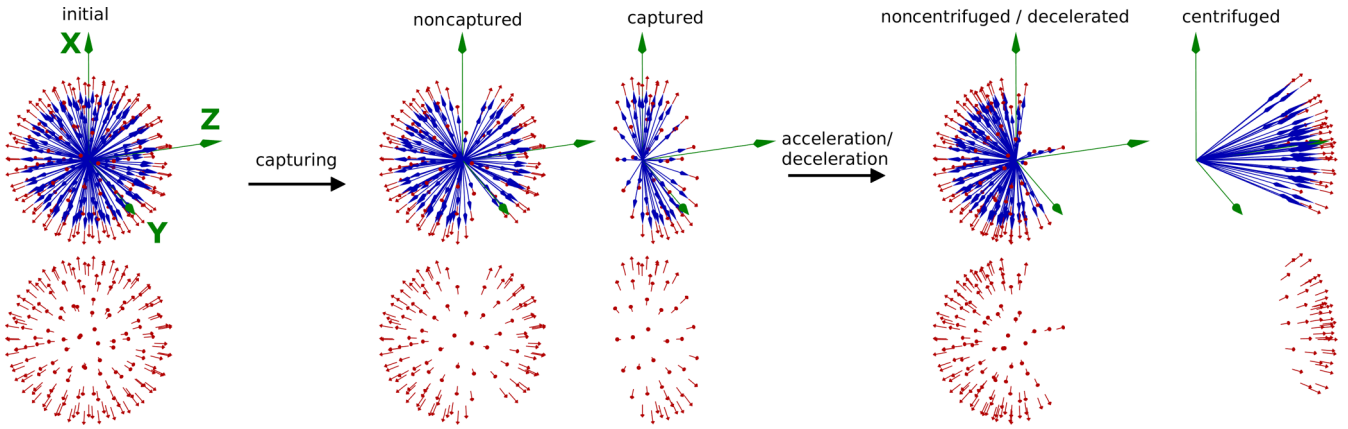

FIG. 4. Classical vector model explaining the polarization of molecules with moderate-to-large initial angular momentum. Long blue arrows depict the orbital angular momentum **N**, whereas short red arrows represent the electronic spin **S**. For clarity, the latter is shown alone in the lower row. K_+ states are considered as an example, i.e., **N** and **S** are parallel. The distribution of the angular momentum in the initial ensemble is isotropic (left part of the figure). In the center, captured and noncaptured molecules are shown separately before the centrifuge spins the former. After the spinning is complete, the two distributions transform into the ones shown on the right.

the K_+ state, for which the spin and rotational angular momentum are parallel (a full quantum mechanical treatment is provided in Appendix B 1). Because of the relatively strong spin-rotational coupling and the weak mixing of the three spin states at $N = 11$, the spin follows the laser-induced orientation of the rotational angular momentum **N** adiabatically. Thus, as the direction of **N** of the captured molecules tilts toward the positive Z direction, **S** follows suit and the K_+ subset of the initial ensemble acquires positive spin polarization. The noncaptured rotors of the K_+ subset, on the other hand, acquire a negative spin polarization caused by a "hole" in the distribution of their angular momentum. The hole is due to the higher probability to capture a molecule initially rotating in the direction of the centrifuge (see Appendix B 1). Molecules with initially antiparallel **S** and **N** (K_- state, not pictured) generate spin polarization in the opposite direction, negative for the centrifuged molecules and positive for the noncentrifuged ones. Finally, the K_0 subset for which **S** and **N** are perpendicular does not produce any spin polarization. Because of the (almost) equal amount of K_+ and K_- molecules at the $N = 11$ level, the net result is $\langle M_S \rangle \approx 0$ for both the centrifuged and noncentrifuged molecules. We therefore conclude that initially fast rotating molecules cannot account for the nonzero polarizations shown in Fig. 3.

On the other hand, consider slow rotors with an initial rotational angular momentum of $N = 1$. Although an adiabatic following of **N** by the electronic spin **S** is not expected at such low values of N, the qualitative picture described above for higher N's still holds (see Appendix B 2 for rigorous quantum calculations supporting this statement). Namely, centrifuged molecules in the K_+ state become positively spinpolarized, whereas K_- rotors acquire negative polarization. However, in contrast to levels with large values of N, in the case of $N = 1$ the three spin states have very different multiplicities: five for K_+ ($J = 2$), three for K_0 ($J = 1$), and only one for K_- ($J = 0$). This fact leads to significantly different thermal populations of the three K states, with 56% of all $N = 1$ molecules residing in K_+ and only 11% in K_-. As a result, the net spin polarization of the molecules centrifuged up from the initial $N = 1$ does not average to zero. Similarly, a nonzero net negative polarization arises from the noncentrifuged slow rotors due to the negatively polarized hole created by the centrifuge in the distribution of their angular momentum. Therefore, low N levels with unbalanced contributions from K_+ and K_- states are responsible for the separation of spin polarization shown in Fig. 3.

These theoretical results are in conflict with our earlier experimental findings reported in Ref. [12]. Whereas the calculations indicate rather small negative spin polarization, present immediately at the end of the centrifuge, the experimental data reveal higher positive polarization arising on a nanosecond timescale after the laser pulse. Below we propose and evaluate numerically a simple model, in which intermolecular collisions are responsible for the experimentally detected behavior.

III. SPIN POLARIZATION IN THE PRESENCE OF COLLISIONS

Earlier theoretical studies of rotational relaxation emphasized the propensity of collisions to conserve the orientation of the molecular angular momentum [22]. Similar to their macroscopic counterparts, molecular gyroscopes maintain the orientation of their rotational axis as they lose rotational energy to the translational degree of freedom. Highly excited super-rotors are significantly more robust against collisions than more slowly rotating molecules [5,23]. Previous experiments confirmed that with increasing angular momentum, the decay times of rotational coherence and rotational orientation become longer [4,24]. This observation suggests that the lifetime of the positive spin polarization, carried by fast super-rotors, should also be longer than the lifetime of the negatively polarized hole imprinted on slow noncentrifuged molecules. Indeed, as the absolute value of N decays, so does the strength of the spin-rotation coupling **NS**, responsible for the orientation of the electronic spin. Faster depolarization of noncentrifuged molecules by collisions may therefore lead to the appearance of the positive polarization observed in the experiment [12].

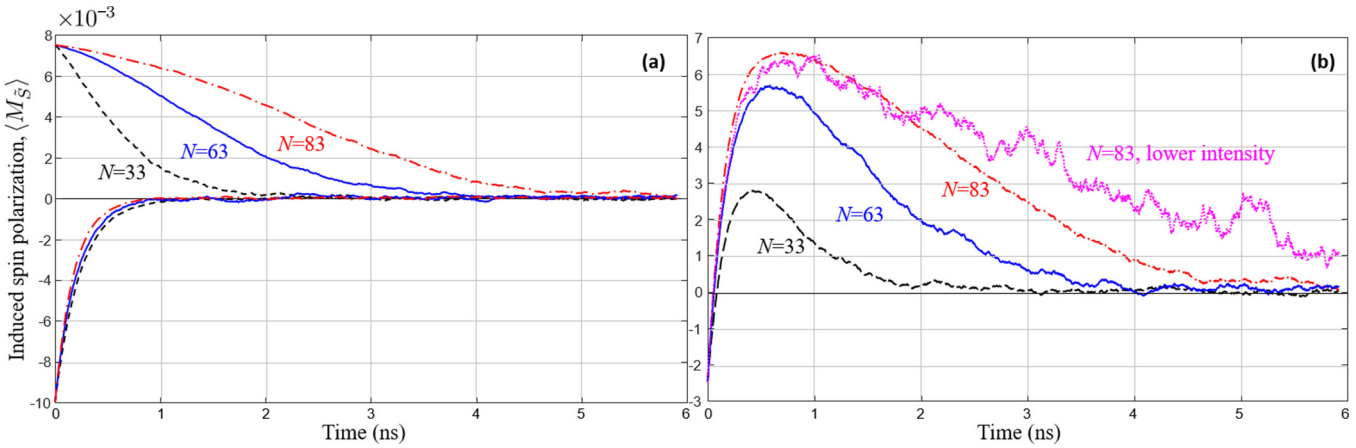

FIG. 5. Numerically calculated magnetization of oxygen gas at $T = 295\,\mathrm{K}$, $P = 90\,\mathrm{kPa}$ in the presence of collisions and for three levels of rotational excitation: $N = 33$ (dashed black lines); $N = 63$ (solid blue lines), and $N = 83$ (dash-dotted red lines). Peak intensity of the centrifuge field is 2 $\mathrm{TW/cm^2}$ and $t = 0$ marks the end of the pulse. (a) Separate contributions to the total magnetization from centrifuged ($\langle M_{\tilde{S}}\rangle_c$, upper curves with positive values) and noncentrifuged ($\langle M_{\tilde{S}}\rangle_n$, lower curves with negative values) O_2 molecules. (b) Total magnetization of the whole molecular ensemble for the same three levels of rotational excitation. The dotted magenta line shows the result for $N = 83$ but at a lower centrifuge peak intensity of 0.5 $\mathrm{TW/cm^2}$ (see Sec. V for the discussion of the intensity dependence).

A. Theoretical model and numerical methods

To investigate the effect of collisions on the magnetization of O_2 molecules, we employed classical molecular dynamics simulations (CMDS), which have been described in detail in an earlier publication [23]. Briefly, the center-of-mass velocities and rotational frequencies of oxygen molecules are first initialized according to the Boltzmann statistics, while their locations and orientations at time zero are randomized uniformly. Next, we calculate the evolution of molecular positions and momenta under external forces and torques using classical equations of motion. The torque exerted on a molecule by the electric field of the centrifuge is calculated as a cross product of the electric field (5) and the induced dipole moment, found according to the instantaneous orientation of the molecular axis and the known polarizability tensor [22,23]. The same values of the centrifuge intensity ($I_0 = 2\,\mathrm{TW/cm^2}$) and frequency chirp ($\beta = 0.52 \times 10^{24}\,\mathrm{s^{-2}}$) as in Sec. II are used to match the experimental conditions. For collisions, the force and the torque are computed using the known O_2-O_2 intermolecular potential, which proved adequate in previous successful CMDS predictions of oxygen absorption line shapes [25,26].

To simulate the magnetization of the centrifuged gas, to each molecule in the ensemble we assigned a classical magnetic moment $\tilde{\mathbf{S}}$ with three possible projections on the rotational axis, $\tilde{S}_N = \pm 1, 0$. The values of $\tilde{S}_N$ were selected in such a way as to reproduce the distribution of the quantum population among the K_-, K_0, and K_+ states for the corresponding rotational level N. Here, N is determined as an odd-valued integer for which the quantized rotational energy of a molecule $N(N+1)\hbar^2/(2I)$ (where I is the moment of inertia) is the closest to its classical rotational energy. In the ensuing classical evolution, we assumed that neither field-free molecular dynamics nor molecular collisions change the projection $\tilde{S}_N$ of $\tilde{\mathbf{S}}$ on the direction of the rotational angular momentum $\mathbf{N}$. Both assumptions are verified by quantum calculations in Appendixes B 1 and C, respectively, where we show that the rate of population exchange between the $K_{\pm,0}$ sublevels is negligible for all but the lowest rotational states.

B. Theoretical results: *Collision-induced* spin polarization

Similarly to the quantum calculations in Sec. II, we calculated the ensemble averaged projection of the classical magnetic moment $\tilde{\mathbf{S}}$ on the laboratory Z axis separately for centrifuged and noncentrifuged molecules ($\langle M_{\tilde{S}}\rangle_c$ and $\langle M_{\tilde{S}}\rangle_n$, respectively). The dependence of both quantities on time t (with $t = 0$ marking the end of the centrifuge pulse) is shown in Fig. 5(a). In agreement with the quantum results shown in Fig. 3, by the end of the centrifuge pulse super-rotors are positively polarized (three curves originating from the upper left corner), whereas the polarization of noncaptured molecules is negative (three curves originating from the lower left corner). We note, however, that CMDS fails to reproduce the exact value of the magnetic moment associated with centrifuged and noncentrifuged molecules, mainly because of the neglected spin-rotation coupling, which plays an important role in the early stage of the interaction with the centrifuge field. To proceed with the classical simulations, we therefore renormalize the initial values of $\langle M_{\tilde{S}}\rangle_c$ and $\langle M_{\tilde{S}}\rangle_n$ at $t = 0$ to those obtained in our quantum analysis, i.e., 7.5×10^{-3} and -10^{-2}, respectively (see Fig. 3). With this renormalization of the initial values, CMDS enables us to follow in time the dynamics of both contributions to the total magnetic moment.

The effect of collisions is reflected by the decay of both $\langle M_{\tilde{S}}(t)\rangle_c$ and $\langle M_{\tilde{S}}(t)\rangle_n$. Not surprisingly, the magnetic moment of noncentrifuged molecules relaxes to zero with a time constant τ_n that does not depend on the rotational state of super-rotors, which represent the minority of the ensemble. Since τ_n describes how fast the orientation of the molecular angular momentum (and hence, of the magnetic moment "attached" to it) is randomized, one would expect it to be similar to the collisional decay time of the molecular alignment. The latter can be deduced from the spectral pressure broadening

coefficient γ as $\tau_{\text{align}} = 1/(\pi c \gamma)$ where c is the speed of light [22]. For oxygen at 90 kPa (used in our CMDS), the known value of γ [25] yields $\tau_{\text{align}} = 0.21$ ns. From the three lower curves in Fig. 5(a), the retrieved time constant $\tau_n \approx 0.2$ ns is in excellent agreement with the above estimate.

In contrast to the magnetic moment of noncentrifuged molecules and in line with our expectation from the gyroscopic effect, the magnetization of super-rotors decays on a longer timescale. The corresponding decay time τ_c increases with the rotational angular momentum N and can reach a few nanoseconds, as illustrated by the upper curves in Fig. 5(a). The significant difference between τ_n and τ_c results in the evolution of the total magnetic moment, $\langle M_{\tilde{S}}(t)\rangle \equiv \langle M_{\tilde{S}}(t)\rangle_c + \langle M_{\tilde{S}}(t)\rangle_n$, depicted in Fig. 5(b). Comparing the CMDS results obtained for $P = 90$ kPa and 45 kPa (not shown) confirmed the inverse proportionality of the decay constants with pressure, as expected from the binary nature of intermolecular collisions at subatmospheric pressures. As we show in Sec. IV below, these results are in good qualitative agreement with our experimental findings.

IV. COMPARISON WITH EXPERIMENT

A. Experimental setup

Our experimental setup is shown in Fig. 6 and is identical to that used in Ref. [12]. Centrifuge pulses, prepared according to the original recipe of Karczmarek *et al.* [1], are amplified in a home-built multipass Ti:sapphire amplifier and focused with a $f = 1000$ mm lens inside a hermetic chamber filled with oxygen at room temperature and variable

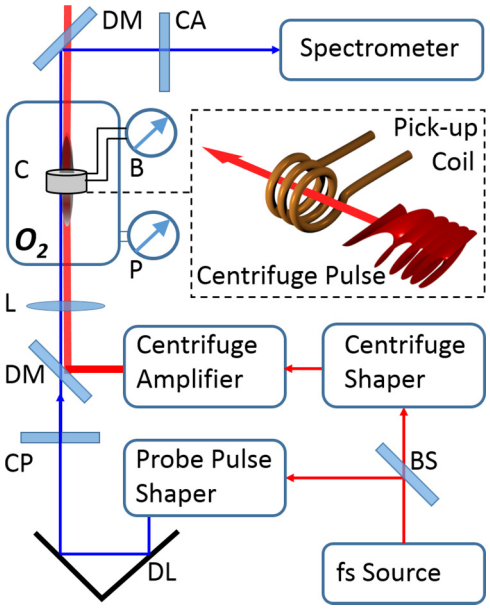

FIG. 6. Experimental setup. BS, beam splitter; DM, dichroic mirror; CP (CA), circular polarizer (analyzer) for right (left) circular polarization; DL, delay line; L, lens; C, pickup coil surrounding the centrifuged volume (dark ellipsoid) and connected to a fast oscilloscope for measuring the magnetic field (B). "O_2" marks the pressure chamber filled with oxygen gas under pressure P at room temperature. An optical centrifuge pulse passing along the axis of a pickup coil is illustrated in the inset.

pressure. From the measured pulse energy and beam diameter, we estimate that the peak intensity of the centrifuge is $I_0 = 2\,\text{TW/cm}^2$. From the cross-correlation frequency-resolved optical gating scan, we extract the frequency chirp, defined in Eq. (6), of $\beta = 0.52 \times 10^{24}\,\text{s}^{-2}$.

To determine the degree of rotational excitation, we use coherent Raman spectroscopy. The latter is executed by sending a weak narrow-band probe pulse through the gas of centrifuged O_2 molecules and measuring the rotation-induced Raman shift, which can be translated to the rotational quantum number of the excited rotational level [27,28]. In Fig. 2(d), a color-coded rotational Raman spectrum is plotted as a function of the time delay between the centrifuge and probe pulses. Owing to the interaction with the centrifuge field, the molecules are climbing up the rotational ladder (bright diagonal trace). Beyond the centrifuge pulse, i.e., at $t > 30$ ps, the broad wave packet with $7 \lesssim N \lesssim 25$ corresponds to the noncentrifuged molecules, whereas the bright trace at $N = 33$ represents the coherent response from the centrifuged super-rotors.

The magnetization of oxygen gas was detected with a pickup coil (1.2-mm diameter, 4.5 turns), centered at the location of the centrifuged volume and coaxial with the centrifuge beam (see inset in Fig. 6). The coil was connected to a 3-GHz bandwidth oscilloscope, which recorded the time-dependent electromotive force (EMF) $\mathcal{E}(t)$. The latter is proportional to the time derivative of the induced magnetization $\mathbf{M}_\parallel$ parallel to the direction of the centrifuge. The molecular spin polarization, responsible for the induced magnetic moment, can therefore be extracted from the detected EMF as

$$\langle M_S\rangle(t) = -c_\parallel \int_{-\infty}^{t} \mathcal{E}(t')dt', \tag{10}$$

with the coefficient $c_\parallel$ determined by the parameters of the coil [12].

B. Experimental results

In dense gases under atmospheric (or comparable with atmospheric) pressure, experimentally observed reorientation times of the super-rotors' high angular momentum are on the scale of a few nanoseconds [6]. The centrifuge-induced magnetic moment, found in Ref. [12], decays on a similar timescale, which supports the proposed connection between the two observables. Here, we investigate the dependence of this decay on the gas pressure and the degree of rotational excitation. The blue solid curves in both panels of Fig. 7 show the measured magnetic moment of oxygen, centrifuged to an angular momentum of $N = 33$ at $P = 45$ and 90 kPa [Figs. 7(a) and 7(b), respectively]. One can see that both the rising and falling edges of the recorded signals are pressure dependent. To quantify this finding, we fit each polarization signal by a sum of two exponentially decaying functions (black dashed lines),

$$P(t) = P_c e^{-t/\tau_c} + P_n e^{-t/\tau_n}, \tag{11}$$

where $P_c > 0$ ($P_n < 0$) is the polarization of the centrifuged (noncentrifuged) molecules right after the laser pulse and τ_c (τ_n) is its decay time. The decay times are listed in the corresponding boxes in Fig. 7. The decrease of both τ_c and

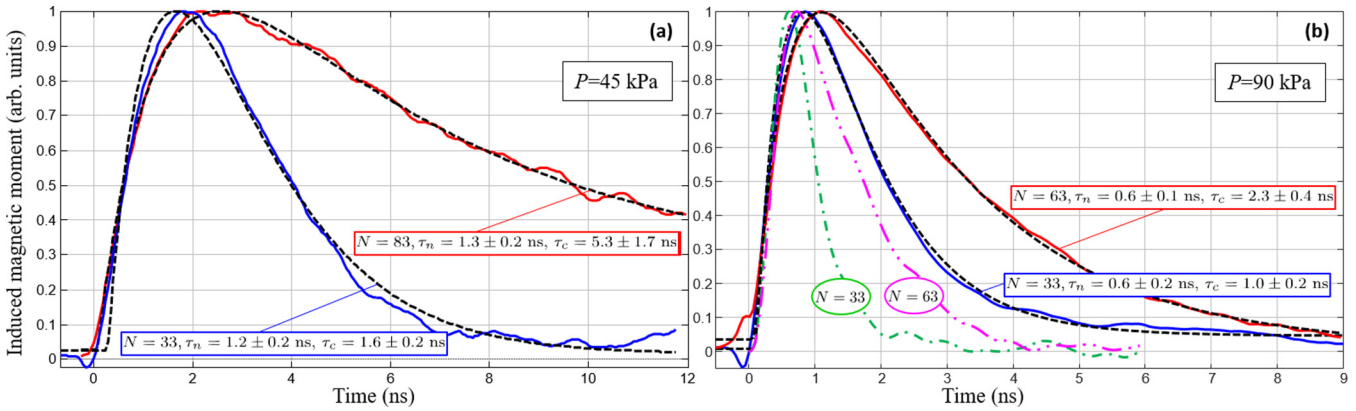

FIG. 7. Experimentally observed dynamics of the induced magnetic moment in the gas of oxygen superrotors at pressures $P = 45$ kPa (a) and $P = 90$ kPa (b). Solid blue (faster decaying) curves on both plots correspond to the rotational angular momentum $N = 33$, whereas solid red (more slowly decaying) curves are for $N = 83$ (a) and $N = 63$ (b). Dashed black lines are best fits to a sum of two exponential functions with the time constants indicated inside corresponding rectangles. The two dash-dotted lines in panel (b) are numerically calculated line shapes from Fig. 5(b), to which a low-pass filter with a cutoff frequency of 1 GHz has been applied in order to simulate the finite time response of our experimental detector.

τ_n (at the fixed value of $N = 33$) in inverse proportionality to the increasing pressure is indicative of the collisional nature of the induced magnetization.

To further validate the suggested model, we investigated the behavior of the observed magnetic moment on the degree of rotational excitation. Red solid curves in Fig. 7 show the experimental signals for higher centrifuge frequencies and correspondingly higher values of the molecular angular momentum. Both at 45 kPa in Fig. 7(a) and 90 kPa in Fig. 7(b) we notice the same result: Since the rising edge of the signal is related to the noncentrifuged molecules, it changes little with increasing N (up to the uncertainty in determining the best fitting parameters, $\tau_n \approx 1.2$ ns for both $N = 33$ and $N = 83$ at $P = 45$ kPa, and $\tau_n \approx 0.6$ ns for both $N = 33$ and $N = 63$ at $P = 90$ kPa). On the other hand, the decay of the positive component of the total polarization, carried by the super-rotors, should exhibit much stronger dependence on their angular momentum, as indeed observed in our experiments (compare τ_c for the two curves within each panel).

V. DISCUSSION AND CONCLUSIONS

Combining the results of quantum calculations from Sec. II, classical simulations from Sec. III, and experimental observations from Sec. IV, we can draw the following conclusions on the nature of the induced spin polarization. On a timescale of the laser pulse (<100 ps), which is shorter than the average time between collisions under considered conditions, molecular interaction with an optical centrifuge results in a separation of magnetic moments: Rotationally excited super-rotors are spin polarized in the (positive) direction of their angular momentum, whereas noncentrifuged molecules are left with an opposite (negative) spin polarization. Owing to the spin dynamics driven by the spin-rotation coupling, the net magnetic moment of the whole ensemble is not zero but slightly negative. Experimental detection of this negative magnetization on such a short timescale was not reliable due to the longer response time of our instrumentation.

On a longer (nanosecond) timescale, beyond the duration of the centrifuge pulse, field-free molecular dynamics in the absence of collisions cannot explain the appearance of the experimentally observed positive magnetization. Intermolecular interactions, on the other hand, can affect the spin polarization in two ways, either via collision-induced spin flipping or through reorienting the molecular angular momentum, which is accompanied by the corresponding reorientation of the spin. Our quantum analysis showed that the probability of spin-flipping collisions is negligibly low at all but the lowest rotational levels, rendering the first option unlikely. On the contrary, classical simulations of the collision-induced rotational reorientation supported the second mechanism. Here, the propensity of collisions to preserve the direction of the rotational axis, i.e., the gyroscopic effect, means that noncentrifuged molecules with low angular momentum will lose their magnetic moment much more quickly than super-rotors, whose positive magnetization will therefore become dominant. The difference between the two relaxation timescales proved sufficient to reproduce the experimental results qualitatively, as can be seen by comparing Figs. 5(b) and 7(b).

Quantitative comparison reveals that both the rise and decay time constant of the experimentally observed magnetization are longer than those calculated numerically. The longer rising time stems from the limited response time of our detector. As shown in Fig. 7(b), by applying an appropriate low-pass filter to the CMDS results, we achieve good agreement between the numerical and experimental rising edges. For the falling edge, we attribute the disagreement to a number of factors. First, the simulations tend to overestimate the density of molecular super-rotors for a given centrifuge intensity. High super-rotor density results in the correspondingly higher heat release and rising gas temperature, followed by the increasing collision rate and avalanche-like accelerated relaxation [5]. The nonexponential decay of the computed magnetization in Fig. 5 is a clear signature of such behavior. To check this conclusion, we studied numerically the dependence of the rotational relaxation rate on the strength, and hence the trapping efficiency, of the centrifuge. The result

of this analysis is shown in Fig. 5(b). The dotted magenta line represents the total magnetization of the molecular ensemble centrifuged to $N = 83$ by a less intense centrifuge (0.5 instead of 2 TW/cm^2). Despite the higher noise level due to the lower density of super-rotors and, therefore, poorer statistics, the effect of slower decay rate at lower intensity is rather clear. We therefore conclude that any decrease in the efficiency of the rotational excitation, such as the nonuniform spatial distribution of the centrifuge beam (specifically, its low intensity wings) and possible propagation effects (e.g., loss of coherent propagation due to filamentation), will indeed result in longer decay times of the induced magnetization. The second reason for the disagreement could be attributed to the fact that classical calculations tend to overestimate the rate at which the molecules reach thermal equilibrium. This is because of the classically allowed noninteger changes of the rotational angular momentum (in units of $\hbar$) which are quantum mechanically forbidden. Finally, the rotational relaxation of super-rotors requires strong intermolecular interactions in which the collision partners get close to one another. Hence, the results of numerical calculations are sensitive to the interaction potential, which may not be accurate enough at short distances.

To summarize, we analyzed a number of possible mechanisms leading to the appearance of a macroscopic magnetic moment, and correspondingly large magnetic field, in a gas of optically centrifuged oxygen molecules. Collision-induced magnetization, based on the molecular gyroscopic effect in combination with strong spin-rotational coupling, was identified as the most likely reason for the discovered effect, which may find future applications in ultrafast magnetic switching and remote magnetic sensing.

ACKNOWLEDGMENTS

We would like to thank Aleksey Korobenko and Ilya Sh. Averbukh for stimulating and insightful discussions on the topic of the manuscript. This research has been supported by the grants from Canada Foundation for Innovation (CFI), British Columbia Knowledge Development Fund (BCKDF), and Natural Sciences and Engineering Research Council of Canada (NSERC).

APPENDIX A: NUMERICAL METHODS FOR CALCULATING THE MOLECULAR WAVE FUNCTION DURING THE INTERACTION WITH THE CENTRIFUGE

For the numerical treatment of the molecule-centrifuge interaction, it is convenient to work in Hund's case (b) basis [13,14]. In this case, the electronic spin **S** is coupled to the orbital angular momentum **N** to form the total angular momentum **J**. The basis functions can be denoted as

$$|\phi\rangle = |\eta, \Lambda; N, \Lambda; N, S, J, M\rangle . \tag{A1}$$

Here, η is a collective quantum number for the vibrational state, Λ is the projection of the electronic orbital angular momentum on the molecular axis, and M is the projection of the total angular momentum on the space-fixed Z axis. Since η, $\Lambda = 0$, and $S = 1$ are constant, in the following the short notation $|\eta, \Lambda; N, \Lambda; N, S, J, M\rangle \equiv |JNM\rangle$ is used. The rotational Hamiltonian is diagonal in Hund's case (b) basis, and the matrix elements are

$$\langle NJM|\mathcal{H}_{\rm rot}|NJM\rangle = B_0 N(N+1) - DN^2(N+1)^2. \tag{A2}$$

The eigenfunctions $|\psi_n\rangle$ and eigenenergies E_n of the effective Hamiltonian (1) are calculated by means of numerical diagonalization.

It is convenient to expand $|\Psi\rangle$ using the eigenfunctions $|\psi_n\rangle$ and eigenvalues E_n of $\mathcal{H}_{\rm eff}$:

$$|\Psi(t)\rangle = \sum_n C_n(t) e^{-iE_n t/\hbar} |\psi_n\rangle . \tag{A3}$$

Inserting (7) and (A3) into (8) yields a set of coupled differential equations for the expansion coefficients,

$$\frac{\partial C_n(t)}{\partial t} = \frac{1}{i\hbar} \sum_m C_m(t) e^{-i(E_m - E_n)t/\hbar} \langle \psi_n | V(t) | \psi_m \rangle . \tag{A4}$$

The temporal envelope of the electric field is assumed to be of the following shape:

$$\mathcal{E}^2(t) = \begin{cases} \sin^2\left[\pi \frac{t}{2t_{\rm on}}\right] & \text{for} \quad 0 \leqslant t < t_{\rm on} \\ 1 & \text{for} \quad t_{\rm on} \leqslant t < t_{\rm p} - t_{\rm off} \\ \sin^2\left[\pi \frac{(t-t_{\rm p})}{2t_{\rm off}}\right] & \text{for} \quad t_{\rm p} - t_{\rm off} \leqslant t < t_{\rm p} \\ 0 & \text{otherwise} \end{cases}, \tag{A5}$$

where $t_{\rm p}$ is the duration of the laser pulse and $t_{\rm on}$ and $t_{\rm off}$ are the turn-on and turn-off times of the pulse, respectively. Note that the intensity of the laser field is assumed to be constant between $t_{\rm on}$ and $t_{\rm off}$, which simplifies the model. In a real experiment, the field envelope is slowly decaying in time toward the end of the pulse.

Using (7) and (A5), the interaction potential can be written as

$$V(t) = -U_0 \mathcal{E}^2(t) \left[r_x^2 \cos^2\left(\beta \frac{t^2}{2}\right) + r_x r_y \cos\left(2\beta \frac{t^2}{2}\right) + r_y^2 \sin^2\left(\beta \frac{t^2}{2}\right) \right].$$

The following relations can be used to express $V(t)$ in terms of the rotation matrices $D^{(j)*}_{mk}$:

$$r_x^2 = \frac{1}{3} - \frac{1}{3} D^{(2)*}_{00} + \frac{1}{\sqrt{6}} D^{(2)*}_{20} + \frac{1}{\sqrt{6}} D^{(2)*}_{-20}, \tag{A6a}$$

$$r_y^2 = \frac{1}{3} - \frac{1}{3} D^{(2)*}_{00} - \frac{1}{\sqrt{6}} D^{(2)*}_{20} - \frac{1}{\sqrt{6}} D^{(2)*}_{-20}, \tag{A6b}$$

$$r_x r_y = -\frac{i}{\sqrt{6}} D^{(2)*}_{20} + \frac{i}{\sqrt{6}} D^{(2)*}_{-20}. \tag{A6c}$$

The matrix elements of the rotation matrices in Hund's case (b) basis are given as

$$\langle JNM|D^{(2)*}_{m0}|JNM\rangle = (-1)^{J+J'-M+1} \sqrt{(2J+1)(2J'+1)(2N+1)(2N'+1)} \times \begin{pmatrix} J & 2 & J' \\ -M & m & M' \end{pmatrix} \begin{pmatrix} N & 2 & N' \\ 0 & 0 & 0 \end{pmatrix} \begin{Bmatrix} N' & J' & 1 \\ J & N & 2 \end{Bmatrix}. \tag{A7}$$

Mapping (A7) to the eigenbasis $|\psi_n\rangle$ of the effective Hamiltonian and using (A6), one obtains the matrix elements $\langle\psi_n|V(t)|\psi_m\rangle$ of the laser-induced potential. Finally, the coupled differential equations (A4) are solved numerically to obtain $|\Psi(t)\rangle$. Note that the coefficients $C_n(t)$ are constant after the turn-off time of the centrifuge pulse, leaving the wave function to evolve as

$$|\Psi(t > t_p)\rangle = \sum_n C_n(t_p) e^{-iE_n t/\hbar} |\psi_n\rangle . \tag{A8}$$

Thermal effects are included via ensemble averaging. Namely, Eq. (A4) is solved for all thermally populated states $|\psi_n\rangle$, and the result is averaged using the respective Boltzmann factors as weights. To make the calculation feasible, only 95% of the initial thermal population is included, corresponding to 675 initial $|JNM\rangle$ states.

APPENDIX B: DEPENDENCE OF CENTRIFUGE-INDUCED SPIN POLARIZATION ON THE INITIAL CONDITIONS

In this section, we provide a detailed breakdown of the induced spin polarization in a thermal ensemble between two groups of molecules: Initially quickly rotating molecules (in particular, one of the most populated levels, $N = 11$) and initially slowly rotating molecules ($N = 1, 3$). The analysis will explain the main conclusion, summarized in Sec. II B, which states that only those molecules which initially occupy low rotational states are responsible for the laser-induced separation of spin polarization between centrifuged and noncentrifuged molecules.

1. Spin polarization originating from *fast initial rotation*

We start by considering oxygen molecules that are already rotating moderately quickly before the interaction with the centrifuge pulse, e.g., molecules with an initial orbital angular momentum of $N = 11$. The thermal population of this level is ∼13% at room temperature, divided among the three spin-rotational states K_-, K_0, and K_+ as 3.9%, 4.2%, and 4.6%, respectively. Different weights of the spin states are due to the higher M degeneracy for higher J.

The capturing efficiency of the centrifuge pulse is quantified in Table I. The results are presented for three different initial spin-rotational states separately, outlining the fractions of the molecules which are centrifuged (*cen*), partly centrifuged (*par*), i.e., initially accelerated but lost from the laser trap before the end of the pulse, remaining in the initial N-level (*rem*), and slowed down by the laser pulse (*slo*). Also shown is the average of the three spin-rotational states, weighted by their respective thermal populations. One can see that the spin-rotational splitting has a negligible effect on the interaction with the centrifuge pulse. Furthermore, only one sixth of the molecules is actually accelerated (of which two thirds are lost before reaching the target rotation frequency), yet a third is decelerated. About one half of the molecules is unaffected by the centrifuge.

TABLE I. Probability of capturing the three spin-rotational states of $N = 11$ level by the centrifuge, averaged over the initial orientation of their total angular momentum **J** (i.e., over M), together with their weighted sum ("all"). Shown are the fractions of molecules that are centrifuged (*cen*, final $N > 26$), are partially centrifuged (*par*, $11 < N < 26$), remain unchanged (*rem*, $N = 11$), and are slowed down by the laser (*slo*, $N < 11$).

Spin-rotational state	*cen*	*par*	*rem*	*slo*
K_-	0.055	0.096	0.504	0.345
K_0	0.057	0.108	0.503	0.332
K_+	0.050	0.102	0.504	0.343
All	0.054	0.103	0.504	0.340

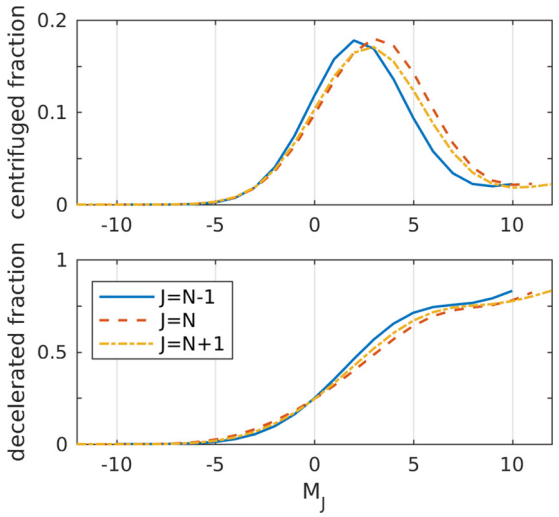

FIG. 8. Probability of a molecule being (a) centrifuged and (b) decelerated as a function of the initial orientation M of the angular momentum **J** with respect to the laser propagation axis, for the three different spin-rotational states of $N = 11$ level.

In Fig. 8, we show the influence of the initial orientation of the angular momentum on the probability to be captured by the centrifuge, again separately for the three spin states. As expected, the centrifuge is most efficient for $M \gtrsim 0$, i.e., for molecules initially rotating slowly in the direction of the forced acceleration. On the other hand, the deceleration is most efficient for molecules already rotating in the same direction as the centrifuge, i.e., with $M \approx J$. Note again that there is no much difference between the three spin-rotational states.

The effect of the laser pulse on the spin polarization is shown in Fig. 9, separately for the three different spin-rotational states in Figs. 9(a)–9(c), and as a thermally weighted average in Fig. 9(d). The solid blue line shows the total spin polarization as a function of time. Dotted vertical lines indicate the time when the angular velocity of the centrifuge equals the initial velocity of the molecules (at $t \approx 12$ ps) and the end of the laser pulse (at $t = 34$ ps). For all three spin-rotational states, the total polarization oscillates with a frequency corresponding to the spin-spin splitting. In contrast to the negative total polarization of a thermal ensemble (Fig. 3), the time-averaged polarization of $N = 11$ state is zero.

A different picture is found when looking at the fully centrifuged molecules (defined by the final orbital angular momentum of $N > 26$) and the noncentrifuged molecules ($N < 26$) separately. Their respective polarizations are

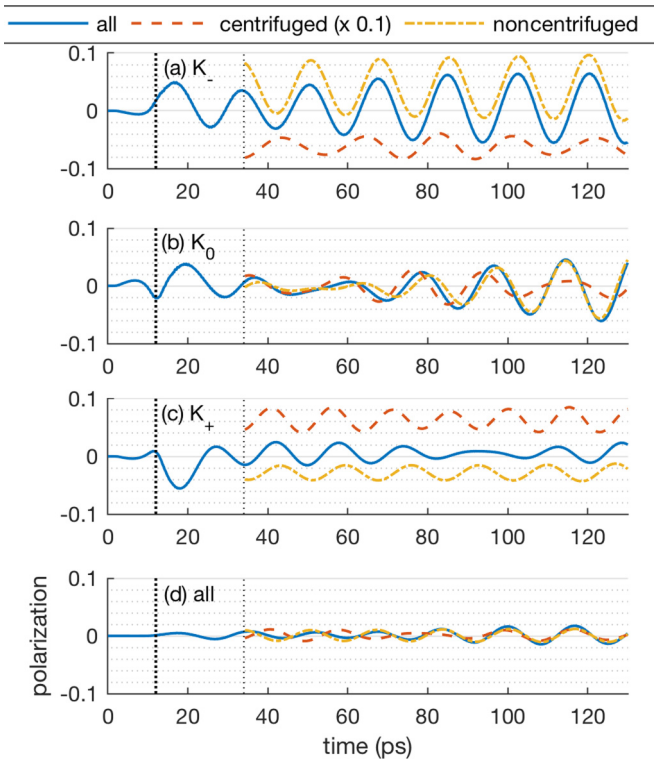

FIG. 9. Polarization of the electronic spin during and after the interaction with the centrifuge pulse. The initial states are the three spin-rotational states of the $N = 11$ level [(a)–(c)], averaged over the orientation of their total angular momentum $\mathbf{J}$ (i.e., over M), together with their weighted sum (d). Shown is the polarization for the whole ensemble (solid blue), as well as its breakdown between centrifuged (red dashed) and noncentrifuged (yellow dot-dashed) molecules, defined as $N > 26$ and $N < 26$, respectively. Note that the polarization of the centrifuged molecules is scaled by a factor of 1/10. The first dotted vertical line indicates when the centrifuge velocity reaches approximately the angular velocity of the $N = 11$ state. The second vertical line indicates the end of the centrifuge pulse.

depicted by red dashed (centrifuged) and yellow dash-dotted (noncentrifuged) lines in Fig. 9. For the K_- initial states, the polarization of the centrifuged molecules is strongly negative, with a time-averaged value of -0.6. This polarization is countered by an opposite polarization of the lower levels, which results in zero overall time-averaged polarization. For the K_+ initial states, the opposite picture is found: Now the centrifuged molecules show positive polarization with an average value of 0.6, and the noncentrifuged molecules are negatively polarized. Again, both polarizations cancel one another. Finally, for K_0, both the centrifuged and noncentrifuged fractions exhibit no net polarization after the time averaging. With each initial K state producing negligible polarization, the net effect of the centrifuge on the spin polarization of $N = 11$ state is correspondingly close to zero.

Finally, we found that there is only a small mixing of the spin-rotational states. Over 90% of the population remains in the initial spin-rotational state, regardless of whether the molecule is centrifuged or not. These results are shown in detail in Table II.

TABLE II. Same as Table I, but showing the distribution among the final spin-rotational states (column *final*) as well as their total population (column $\sum$).

Initial	Final	*cen*	*par*	*rem*	*slo*	$\sum$
K_-	K_-	0.049	0.092	0.477	0.304	0.922
	K_0	0.004	0.003	0.017	0.033	0.057
	K_+	0.002	0.001	0.010	0.008	0.021
K_0	K_-	0.005	0.010	0.018	0.013	0.045
	K_0	0.051	0.094	0.461	0.303	0.908
	K_+	0.001	0.005	0.025	0.016	0.047
K_+	K_-	0.002	0.002	0.009	0.007	0.019
	K_0	0.003	0.007	0.021	0.009	0.040
	K_+	0.045	0.093	0.474	0.327	0.940

From these results, we propose a simple model for the polarization process, using a classical vector picture for the angular momenta. It is known that a centrifuge pulse interacts with linear molecules by keeping the value of $N - M_N$ constant [29], where M_N is the projection of $\mathbf{N}$ onto the laser propagation axis. Thus, as the angular momentum increases, so does the ratio M_N/N. Hence, the orbital angular momentum $\mathbf{N}$ is slowly oriented along the Z axis by the centrifuge. The model now assumes that the electronic spin $\mathbf{S}$ follows the reorientation of the orbital angular momentum $\mathbf{N}$ adiabatically. Consider K_+ state with $\mathbf{S}$ parallel to $\mathbf{N}$, as depicted in Fig. 4. In the beginning, the angular momenta are randomly oriented, as shown in the left panel for a thermal ensemble of molecules. According to the results shown in Fig. 8, the centrifuge pulse captures mostly molecules with $0 < M_J < 5$. Thus, the captured molecules will produce a weak positive polarization.

Among the noncaptured molecules, a "hole" is created because of the missing projections $0 < M < 5$, and since $\mathbf{S}$ is parallel to $\mathbf{N}$, the ensemble of noncaptured molecules is slightly negatively polarized. This is depicted in the center frame of Fig. 4. Finally, after the captured molecules have been accelerated, their rotational angular momentum $\mathbf{N}$ is oriented along the Z axis. The electronic spin following $\mathbf{N}$ leads to a positive polarization of the accelerated molecules. Among the noncaptured molecules, the ones with $M_N \approx N$ have been slightly decelerated, lowering the projection M_N. The electronic spin following $\mathbf{N}$ thus also experiences a lowering of the projection M_S. Together with the polarization from the hole created by the capturing process, this leads to the negative polarization for the noncentrifuged molecules.

For the K_- spin-rotational states, the analysis follows accordingly, though now the electronic spin is antiparallel to $\mathbf{N}$ and thus the signs are reversed. Finally, for the K_0 spin-rotational states, the orientation of $\mathbf{N}$ has no effect on M_S, since the electronic spin is perpendicular to $\mathbf{N}$.

We now test whether the model holds quantitatively. Using $\mathbf{J} = \mathbf{N} + \mathbf{S}$, $|\mathbf{J}| = \sqrt{J(J+1)}$, $|\mathbf{N}| = \sqrt{N(N+1)}$ as well as $|\mathbf{S}| = \sqrt{S(S+1)}$, and the fact that $\mathbf{S}$ and $\mathbf{N}$ precess around $\mathbf{J}$, one obtains for the projection M_S of the spin onto the Z axis (time-averaged over the precession)

$$M_S = M\frac{2 + J(J+1) - N(N+1)}{2J(J+1)}, \qquad \text{(B1)}$$

which simplifies for the three spin-rotational states to

$$M_S^-(J,M) = -\frac{M}{J+1}, \tag{B2a}$$

$$M_S^0(J,M) = \frac{M}{J(J+1)}, \tag{B2b}$$

$$M_S^+(J,M) = \frac{M}{J}. \tag{B2c}$$

Using these expressions, one can calculate the polarization of the centrifuged molecules as

$$\langle M_S^i \rangle_{\text{cen}} = \frac{1}{F_C} \sum_M M_S^i(J+\Delta N, M+\Delta N) f_c(M), \tag{B3}$$

where i denotes the spin-rotational state, ΔN is the orbital angular momentum change induced by the centrifuge, $f_c(M)$ is the probability of a molecule in state M being centrifuged, and $F_c = \sum f_c(M)$ is a normalization factor. Plugging in $\Delta N = 20$ and the numerical values for $f_c(M)$ (see Fig. 8), one finds that the model predicts a polarization of -0.73 for K_-, 0.02 for K_0, and 0.73 for K_+. The values predicted by this classical vector model are 10–20% larger than those observed in the full quantum mechanical simulations; see Fig. 9. Considering that the model neglects the 5–10% of molecules that undergo a spin flip during the centrifuge pulse, which lowers the final polarization, this difference seems reasonable.

Concluding this part, the centrifuge induces a polarization of the electronic spin for initially quickly rotating molecules, if the molecules are in either K_+ or K_- spin-rotational state. The polarization is likely due to the fact that the centrifuge reorients the orbital angular momentum, while the electronic spin follows adiabatically. The polarizations of the two spin states are of almost equal magnitude and opposite sign. Therefore, neither centrifuged nor noncentrifuged molecules exhibit any significant residual spin polarization by the end of the laser pulse.

2. Spin polarization originating from *slow initial rotation*

There are three major differences between initially slow and fast rotating molecules. First, for low N the three spin states have significantly different multiplicities: For $N = 1$ and $J = 2$, there are five different orientations $M_J = 0, \pm1, \pm2$, whereas for $N = 1$ and $J = 0$ there is only one orientation $M_J = 0$, which leads to significantly different thermal populations. For instance, at room temperature, 56% of the $N = 1$ population resides in K_+ and only 11% in K_-. Second, at low N the mixing of the spin-rotational states is much stronger, making the electronic spin more likely to flip instead of following **N** adiabatically. Third, the centrifuge is more efficient in exciting low rotational levels to super-rotor states. Given these differences, it seems likely that the centrifuge-induced spin polarization for initially slow molecules may differ from the polarization of initially fast rotors.

In this section, molecules with initial orbital angular momenta of $N = 1$ and $N = 3$ are considered. At room temperature, only 4% and 9% (for $N = 1$ and $N = 3$, respectively) of the thermal population resides in these levels. Yet the probability of being captured by the centrifuge, shown in Table III, is rather high for these slow rotors: 60% for $N = 1$ and 23% for $N = 3$ (much higher than the 5% probability found for $N = 11$). As a result, approximately 25% of the centrifuged population in a room temperature thermal ensemble arises from the $N = 1$ states, and a further 20% from $N = 3$. From the data in Table III it can also be seen that similarly to the higher N levels, the efficiency of the centrifuge is almost independent from the initial spin-rotational state.

TABLE III. Efficiency of the centrifuge pulse for the three spin-rotational states of $N = 1$ and $N = 3$ levels, averaged over the initial orientation of the angular momentum **J** (i.e., over M). Shown is the final population of centrifuged molecules (*cen*), partially centrifuged (*par*), molecules with no change of the orbital angular momentum (*rem*), and slowed down molecules (*slo*). Molecules are considered centrifuged when their final orbital momentum is larger than $N = 26$.

	Initial	Final			
N	Spin rotational	*cen*	*par*	*rem*	*slo*
1	K_-	0.61	0.18	0.21	
1	K_0	0.55	0.14	0.31	
1	K_+	0.59	0.12	0.29	
3	K_-	0.24	0.10	0.45	0.21
3	K_0	0.23	0.11	0.47	0.19
3	K_+	0.23	0.13	0.46	0.18

We first look at molecules initially occupying $N = 1$ level. The polarization of the electronic spin, i.e., the expectation value $\langle M_S \rangle$, is plotted in Fig. 10. For K_+ and K_-, the same pattern as for the initially fast molecules is found: For K_+, the centrifuged molecules (dashed red line) show positive polarization, while the noncentrifuged ones (dash-dotted yellow line) are negatively polarized. For K_- the signs are reversed. For the initial K_0 spin state, both the centrifuged and the noncentrifuged molecules become negatively polarized, which is a result of nonadiabatic spin flips during the centrifuge action. Importantly, in sharp contrast to the $N = 11$ case, there is a non-negligible net polarization of the centrifuged and noncentrifuged subensembles [Fig. 10(d)] stemming from the big imbalance between the initial populations of K_+ and K_- spin states.

In Table IV, the change of the population in different spin-rotational states of $N = 1$ level is shown in detail. It can be seen that, in contrast to the initially fast spinning molecules, for the initially slow molecules there is a considerable exchange of population between the spin states. Notably, while K_+ and K_- are mixing predominantly with one another, centrifuged K_0 molecules exhibit preferential mixing with K_-, which explains their negative spin polarization at the end of the laser pulse, mentioned in the previous paragraph.

In Fig. 11, the polarization is shown for the molecules initially occupying $N = 3$ levels. The overall picture is the same as for $N = 1$, including the (classically unexpected) polarization of the K_0 state. In contrast to $N = 1$, the ensemble average is now negatively polarized due to the K_+ levels being less dominant (i.e., lower multiplicity imbalance). Here, the positive polarization of K_+ is almost canceled by the negative polarization of K_-, and the additional negative

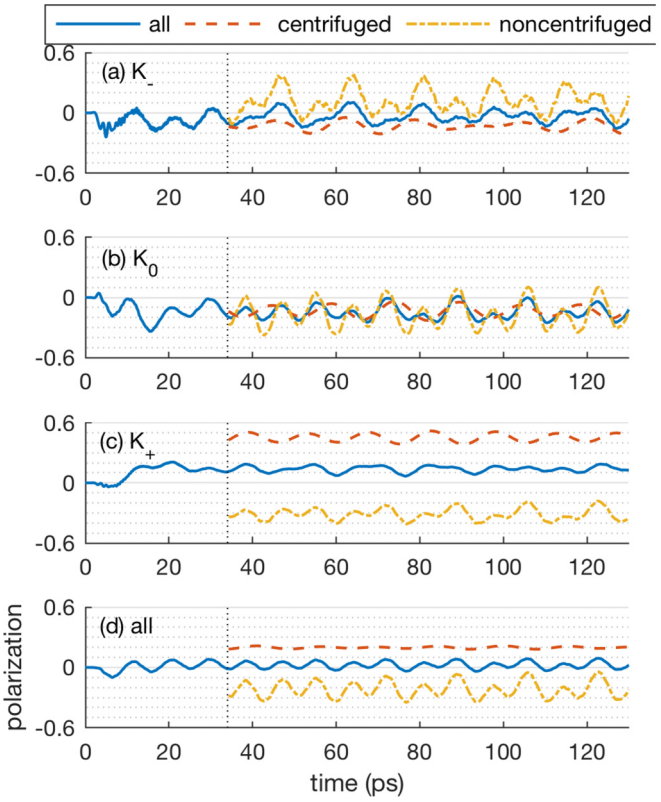

FIG. 10. Polarization of the electronic spin during and after the interaction with the centrifuge pulse. The initial states are the three spin-rotational states of the $N = 1$ level [(a)–(c)], averaged over the orientation of their total angular momentum $\mathbf{J}$ (i.e., over M), together with their weighted sum (d). Shown is the polarization for the whole ensemble (solid blue), as well as its breakdown between centrifuged (red dashed) and noncentrifuged (yellow dot-dashed) molecules, defined as $N > 26$ and $N < 26$, respectively. The dotted vertical line indicates the end of the centrifuge pulse.

polarization of K_0 pushes the ensemble average to a negative net value. As a result, the net polarization of the whole thermal ensemble depends on the relative population and the capturing probability of low initial N levels. At room temperature, the $N = 1$ and $N = 3$ levels account for 4% and 9% of the total

TABLE IV. Same as Table II but for $N = 1$ initial state.

Initial	Final	*cen*	*par*	*rem*	*slo*	$\sum$
	K_-	0.338	0.048	0.043		0.430
K_-	K_0	0.017	0.008	0.016		0.042
	K_+	0.257	0.118	0.153		0.529
	All	0.612	0.178	0.210		1.000
	K_-	0.246	0.058	0.062		0.366
K_0	K_0	0.139	0.042	0.173		0.354
	K_+	0.163	0.040	0.078		0.281
	All	0.548	0.141	0.311		1.000
	K_-	0.119	0.048	0.030		0.197
K_+	K_0	0.083	0.027	0.036		0.146
	K_+	0.387	0.044	0.226		0.657
	All	0.589	0.122	0.289		1.000

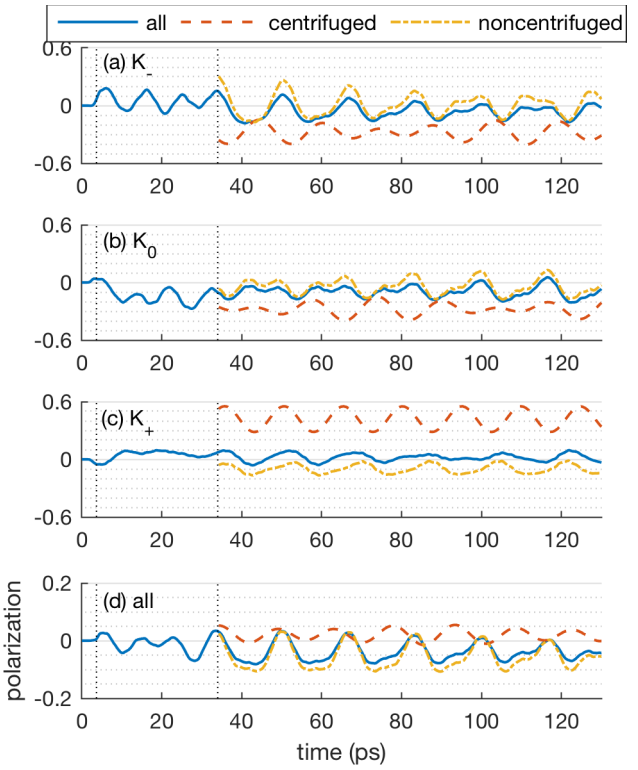

FIG. 11. Same as Fig. 10 but for the initial $N = 3$ state.

population, respectively. According to our calculations, the former is captured with the probability of 60%, whereas it drops to 23% for the latter. The interplay between these two factors leads to the small number of strongly and positively polarized super-rotors and a bigger number of weakly and negatively polarized noncentrifuged molecules, as shown in Fig. 3.

APPENDIX C: COLLISION-INDUCED SPIN DYNAMICS

In this section, we calculate collision cross sections $(N, K) \to (N', K')$, where K and K' $(= K_-1, K_0, \text{or } K_+)$ describe the projection of the electronic spin on the molecular angular momentum as discussed in Sec. II A. We use the energy corrected sudden (ECS) model, which was applied successfully to the description of the line-mixing effects on the spectra of many molecular systems (see Chapter IV of Ref. [30] and references therein) and, in particular, to oxygen absorption in the A-band region [31,32] and microwave region [33].

Within the ECS approach, the cross section for the collision-induced change $(N, J) \to (N', J')$ is given by

$$\begin{aligned}\sigma(N, J \to N', J') &= \sqrt{\frac{[J']}{[J]}}[N][N'][J][J'] \sum_L \begin{pmatrix} N & N' & L \\ 0 & 0 & 0 \end{pmatrix}^2 \\ &\times \begin{Bmatrix} L & J & J' \\ 0 & J' & J \end{Bmatrix} \begin{Bmatrix} L' & J & J' \\ S & N' & N \end{Bmatrix}^2 \\ &\times \frac{\Omega(N)}{\Omega(L)}[L]Q(L), \end{aligned} \tag{C1}$$

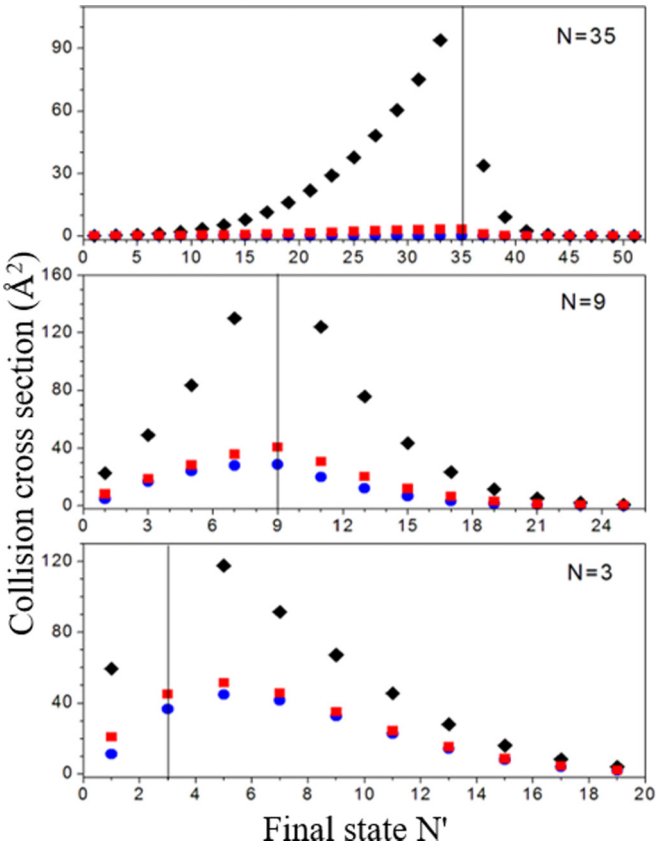

FIG. 12. Collision cross sections $\sigma(N, K_+ \to N', K_-)$ (blue circles), $\sigma(N, K_+ \to N', K_0)$ (red squares), and $\sigma(N, K_+ \to N', K_+)$ (black diamonds) as a function of the final rotational quantum number N' for three values of the initial rotational state (marked with a gray vertical line on the corresponding plot): (a) $N = 35$, (b) $N = 9$, and (c) $N = 3$.

where $S = 1$, $(:::)$ and $\{:::\}$ are $3J$ and $6J$ symbols and $[J] = \sqrt{2J+1}$. $Q(L \neq 0)$ are the cross sections $\sigma(L \to 0)$ for the de-excitation from $J = L$ to $J = 0$ of a hypothetical spinless molecule. The rotation of the molecules during collisions is taken into account through ECS adiabaticity factors, which are given by

$$\Omega(N) = \left[1 + \tfrac{1}{24}(\omega_{N,N-2}\tau_c)^2\right]^{-2}, \tag{C2}$$

where τ_c is the average duration of collisions. Note that Eq. (C2) is used for calculating the cross sections of downward transitions ($N' < N$) only. For the upward transitions, one must apply the detailed balance relationship:

$$\rho_k \sigma(k \to l) = \rho_l \sigma(l \to k), \tag{C3}$$

with ρ_k representing the population of level $k \equiv N, J$. For the calculations performed here, all the required ECS parameters (τ_c and the set of $Q(L)$ cross sections) were taken from Ref. [32].

The results are shown in Fig. 12, where the collision cross section $\sigma(N, J \to N', J')$ is plotted as a function of N' for three values of the initial rotational quantum number, $N = 3, 9$ (representing the noncentrifuged molecules) and $N = 35$ (typical for O_2 super-rotors considered in this work). Without loss of generality, K_+ is taken as the initial spin state, i.e., $J = N + 1$. The figure enables one to compare the efficiency with which collisions change the orientation of the electronic spin ($K_+ \to K_0$ and $K_+ \to K_-$, shown by blue circles and red squares, respectively) versus those in which the spin orientation is conserved ($K_+ \to K_+$, black diamonds). As can be seen from Fig. 12(a), super-rotors (high N) cannot become spin polarized due to collisions, since the cross section for transitions conserving the spin orientation is about three orders of magnitude greater than the cross section for the spin flipping transitions. Only at very low values of N do the three cross sections become comparable. This findings suggests that our classical molecular dynamics simulations (Sec. III A) may slightly underestimate the spin relaxation rate for the noncentrifuged molecules. On the other hand, it supports the main conclusion of this work that the separation of magnetic moments by the centrifuge is the necessary ingredient for generating the observed gas magnetization.

[1] J. Karczmarek, J. Wright, P. Corkum, and M. Yu. Ivanov, Optical Centrifuge for Molecules, Phys. Rev. Lett. **82**, 3420 (1999).

[2] D. M. Villeneuve, S. A. Aseyev, P. Dietrich, M. Spanner, M. Yu. Ivanov, and P. B. Corkum, Forced Molecular Rotation in an Optical Centrifuge, Phys. Rev. Lett. **85**, 542 (2000).

[3] C. Toro, Q. Liu, G. O. Echebiri, and A. S. Mullin, Inhibited rotational quenching in oriented ultra-high rotational states of CO_2, Mol. Phys. **111**, 1892 (2013).

[4] A. A. Milner, A. Korobenko, J. W. Hepburn, and V. Milner, Effects of Ultrafast Molecular Rotation on Collisional Decoherence, Phys. Rev. Lett. **113**, 043005 (2014).

[5] Y. Khodorkovsky, U. Steinitz, J.-M. Hartmann, and I. S. Averbukh, Collisional dynamics in a gas of molecular superrotors, Nat. Commun. **6**, 7791 (2015).

[6] A. A. Milner, A. Korobenko, K. Rezaiezadeh, and V. Milner, From Gyroscopic to Thermal Motion: A Crossover in the Dynamics of Molecular Superrotors, Phys. Rev. X **5**, 031041 (2015).

[7] A. A. Milner, A. Korobenko, J. Floß, I. Sh. Averbukh, and V. Milner, Magneto-Optical Properties of Paramagnetic Superrotors, Phys. Rev. Lett. **115**, 033005 (2015).

[8] A. Korobenko and V. Milner, Dynamics of molecular superrotors in an external magnetic field, J. Phys. B **48**, 164004 (2015).

[9] J. Floß, A theoretical study of the dynamics of paramagnetic superrotors in external magnetic fields, J. Phys. B **48**, 164005 (2015).

[10] B. Friedrich and D. R. Herschbach, On the possibility of aligning paramagnetic molecules or ions in a magnetic field, Z. Phys. D **24**, 25 (1992).

[11] A. Slenczka, B. Friedrich, and D. Herschbach, Pendular Alignment of Paramagnetic Molecules in Uniform Magnetic Fields, Phys. Rev. Lett. **72**, 1806 (1994).

[12] A. A. Milner, A. Korobenko, and V. Milner, Ultrafast Magnetization of a Dense Molecular Gas with an Optical Centrifuge, Phys. Rev. Lett. **118**, 243201 (2017).

[13] C. H. Townes and A. L. Schawlow, *Microwave Spectroscopy* (McGraw-Hill, New York, 1955).

[14] J. Brown and A. Carrington, in *Rotational Spectroscopy of Diatomic Molecules*, edited by R. J. Saykally, A. H. Zewail, and D. A. King (Cambridge University Press, Cambridge, UK, 2003).

[15] M. Tinkham and M. W. P. Strandberg, Theory of the fine structure of the molecular oxygen ground state, Phys. Rev. **97**, 937 (1955).

[16] G. Herzberg, *Molecular Spectra and Molecular Structure, I: Spectra of Diatomic Molecules* (Van Nostrand Reinhold, New York, 1950).

[17] K. P. Huber and G. Herzberg (data prepared by J. W. Gallagher and R. D. Johnson, III), Constants of diatomic molecules, in *NIST Chemistry Webbook, NIST Standard Reference Database Number 69*, edited by P. J. Linstrom and W. G. Mallard (National Institute of Standards and Technology, Gaithersburg, MD).

[18] B. A. Zon and B. G. Katsnelson, Nonresonant scattering of intense light by a molecule, Zh. Eksp. Teor. Fiz. **69**, 1166 (1975) [Sov. Phys. JETP **42**, 595 (1975)].

[19] B. Friedrich and D. Herschbach, Alignment and Trapping of Molecules in Intense Laser Fields, Phys. Rev. Lett. **74**, 4623 (1995).

[20] B. Friedrich and D. Herschbach, Polarization of molecules induced by intense nonresonant laser fields, J. Phys. Chem. **99**, 15686 (1995).

[21] R. W. Boyd, *Nonlinear Optics*, 3rd ed. (Elsevier, Amsterdam, 2008).

[22] J.-M. Hartmann and C. Boulet, Quantum and classical approaches for rotational relaxation and nonresonant laser alignment of linear molecules: A comparison for CO_2 gas in the nonadiabatic regime, J. Chem. Phys. **136**, 184302 (2012).

[23] U. Steinitz, Y. Khodorkovsky, J. M. Hartmann, and I. S. Averbukh, Dynamics and hydrodynamics of molecular superrotors, ChemPhysChem **17**, 3795 (2016).

[24] M. J. Murray, H. M. Ogden, and A. S. Mullin, Anisotropic kinetic energy release and gyroscopic behavior of CO_2 super rotors from an optical centrifuge, J. Chem. Phys. **147**, 154309 (2017).

[25] J.-M. Hartmann, V. Sironneau, C. Boulet, T. Svensson, J. T. Hodges, and C. T. Xu, Collisional broadening and spectral shapes of absorption lines of free and nanopore-confined O_2 gas, Phys. Rev. A **87**, 032510 (2013).

[26] J. Lamouroux, V. Sironneau, J. T. Hodges, and J. M. Hartmann, Isolated line shapes of molecular oxygen: Requantized classical molecular dynamics calculations versus measurements, Phys. Rev. A **89**, 042504 (2014).

[27] O. Korech, U. Steinitz, R. J. Gordon, I. Sh. Averbukh, and Y. Prior, Observing molecular spinning via the rotational doppler effect, Nat. Photon. **7**, 711 (2013).

[28] A. Korobenko, A. A. Milner, and V. Milner, Direct Observation, Study, and Control of Molecular Superrotors, Phys. Rev. Lett. **112**, 113004 (2014).

[29] T. Armon and L. Friedland, Capture into resonance and phase-space dynamics in an optical centrifuge, Phys. Rev. A **93**, 043406 (2016).

[30] J.-M. Hartman, C. Boulet, and D. Robert, *Collisional Effects on Molecular Spectra: Laboratory Experiments and Models, Consequences for Applications* (Elsevier, Amsterdam, 2008).

[31] H. Tran, C. Boulet, and J.-M. Hartmann, Line mixing and collision-induced absorption by oxygen in the a band: Laboratory measurements, model, and tools for atmospheric spectra computations, J. Geophys. Res. **111**, D15210 (2006).

[32] H. Tran and J.-M. Hartmann, An improved O_2 A band absorption model and its consequences for retrievals of photon paths and surface pressures, J. Geophys. Res. **113**, D18104 (2008).

[33] D. S. Makarov, M. Y. Tretyakov, and C. Boulet, Line mixing in the 60-GHz atmospheric oxygen band: Comparison of the MPM and ECS model, J. Quant. Spectrosc. Radiat. Transfer **124**, 1 (2013).